PAPER

Terahertz bremsstrahlung and frequency comb induced by variable motion of an antiferromagnetic domain wall

To cite this article: Xu Ge *et al* 2022 *J. Phys. D: Appl. Phys.* **55** 295302

View the article online for updates and enhancements.

Terahertz bremsstrahlung and frequency comb induced by variable motion of an antiferromagnetic domain wall

Xu Ge[1,3]**, Yangyi Chen**[1,3]**, Yue Cao**[1]**, Can Li**[1]**, Tailin Li**[1]**, Ziquan Li**[1]**, Long You**[1]**, Shiheng Liang**[2] **, Xiaofei Yang**[1] **and Yue Zhang**[1,*]

[1] School of Optical and Electronic Information, Huazhong University of Science and Technology, Wuhan, People's Republic of China
[2] Department of Physics, Hubei University, Wuhan, People's Republic of China

E-mail: yue-zhang@hust.edu.cn

Abstract
We numerically investigate the emission of spin wave (SW) packets from an antiferromagnetic (AFM) domain wall (DW) moving at a *varying* velocity. This SW is analogous to the bremsstrahlung of a charge with variable motion. The SW packets are emitted towards both sides of DW in the DW acceleration/deceleration process. The frequency of this bremsstrahlung-type SW is at sub-terahertz (THz), which is one magnitude lower than that of SW emitted by the Lorentz contraction of DW. Based on the bremsstrahlung-type SW, we proposed a frequency comb with a sub-THz central frequency and a GHz frequency interval by exploiting the back-and-forth DW variable motion. Our work paves a way for developing a spin–orbit-torque -based AFM THz device with a tunable frequency band.

Keywords: bremsstrahlung spin wave, frequency comb, antiferromagnetic domain wall, variable motion

(Some figures may appear in color only in the online journal)

1. Introduction

Spin waves (SWs) are promising information carriers in computation devices that are free from Joule heat [1]. The SW in an antiferromagnetic (AFM) medium is especially outstanding owing to its ultrahigh frequency terahertz (THz) brought by strong exchange coupling [2]. This AFM SW has an important position in the emerging research area of THz magnonics [3].

In an AFM medium, in addition to a simple uniform magnetic structure, complicated magnetic textures are also widely observed. A typical example is a magnetic domain wall (DW) that separates the neighboring domains [4]. The interaction between SWs and DWs effectuates interesting physical phenomena [5–7]. For example, an AFM SW can pass a DW without reflection [5, 6], and an AFM DW moving at a high velocity can be a source for exciting THz SW [7]. In addition to that, nonlinear magnon phenomenon, such as a magnonic frequency comb (MFC), can also be generated by the interaction between SW and a magnetic texture. Here the frequency-comb (FC) indicates a spectrum composed of a series of frequencies with an identical interval [8–14]. For example, a MFC can be generated by the interaction between SW and oscillation DW [13] or by nonlinear magnon-skyrmion scattering [14].

Till now, a number of methods have been proposed to drive an AFM DW, such as spin–orbit-torque (SOT) by electrical current [7, 15, 16], anisotropy gradient under voltage [17], temperature gradient [18–20], and spin waves [6, 21]. Especially, the SOT-induced motion of an AFM or ferrimagnetic DW has attracted extensive attention in recent years due to

---

the experimental feasibility. In physics, an AFM DW motion exhibits interesting relativistic-like characteristics, such as an upper limit of velocity and the shrinking of DW width (Lorentz contraction) [7, 22, 23]. When the DW velocity approaches its limit, the maximum group velocity [$(v_g)_{max}$], a SW can be emitted [7, 23] (named SW-1). On the other hand, an AFM DW also has an effective mass that gives rise to DW inertia [17, 24], and another SW emission is also theoretically predicted by DW variable motion [25]. This SW (labeled as SW-2) is analogous to the bremsstrahlung of a charge, such as x-ray emission by an electron colliding with an atomic nucleus. These investigations predict that a moving AFM DW can be a potential source for the emission of a THz SW.

In a real device, SOT-induced DW motion is usually triggered by a current *pulse*. A period of the pulse includes three stages: rising edge, maintenance, and falling edge. In general, the attention is paid on the SW-1 emission by the DW uniform motion under a constant current in the maintenance stage. However, the prediction for SW-2 reminds us to notice possible SW emission during DW acceleration (deceleration) process in the short rising (falling) edge. In this work, we numerically revealed the transient emission of a SW packet–packet by the AFM DW acceleration (deceleration) in the rising (falling) edge of a current pulse. The frequency of this SW-2 is at THz and one magnitude lower than that of SW-1. Based on this bremsstrahlung-type SW-2 emission, we also propose the generation of a SW FC by exploiting the back-and-forth DW variable motion under a pulsed current.

2. Model and method

We consider an AFM/HM bilayer with a Néel-type DW [7]. Under the injection of a longitudinal DC current along the *x*-axis direction in the HM layer, a transversal spin current with spin pointing along the *y* axis is generated and injected into the AFM layer (figure 1(a)).

This spin current introduces a damping-like SOT that drives the AFM DW. Here, we focus on the DW acceleration (deceleration) and the excitation of SW-2 in the rising (falling) edge of the current pulse (figure 1(b)).

The SOT-induced AFM DW motion is numerically calculated based on a one-dimensional (1D) atomistic model with the Hamiltonian given by [7]:

$$
\begin{aligned}
H = & A_{sim} \sum_i \vec{S}^{(i)} \cdot \vec{S}^{(i+1)} - K_{sim} \sum_i \left(\vec{S}^{(i)} \cdot \vec{e}_z \right)^2 \\
& - D_{sim} \sum_i \vec{e}_y \cdot \left(\vec{S}^{(i)} \times \vec{S}^{(i+1)} \right) \\
& + \frac{\mu_0 M_S \mu}{8\pi} \sum_{i,j} \left(\frac{\vec{S}^{(i)} \cdot \vec{S}^{(j)}}{-\frac{3(\vec{S}^{(i)} \cdot \vec{R}_{ij})(\vec{S}^{(j)} \cdot \vec{R}_{ij})}{R_{ij}^2}} \right),
\end{aligned}
\tag{1}
$$

where $\vec{S}^{(i)}$ is the normalized magnetic moment at lattice site *i*. The first term on the right-hand side of equation (1) denotes the exchange energy, where A_{sim} is the exchange integral. The second term is the anisotropy energy with a constant K_{sim}. The

third term is the interfacial Dzyaloshinskii–Moriya interaction (DMI) energy with a coefficient D_{sim}, which gives rise to a Néel-type DW structure [7]. The last term is the dipole–dipole interaction, where M_s and μ are the saturation magnetization of the sub-lattice and the magnetic moment, respectively, and M_s is given by $M_s = \mu/d^3$ with nearest neighbor spacing *d*. $\vec{R}_{ij}$ is the distance vector between site *i* and *j* (i.e., $R_{ij} = |i - j| d$).

The spin dynamics is described by the Landau–Lifthiz–Gilbert (LLG) equation:

$$
\begin{aligned}
\frac{\partial \vec{S}^{(i)}}{\partial t} = & \gamma \mu_0 \vec{S}^{(i)} \times \vec{H}_{eff}^{(i)} + \alpha \vec{S}^{(i)} \times \frac{\partial \vec{S}^{(i)}}{\partial t} \\
& + \gamma B_D \vec{S}^{(i)} \times (\vec{S}^{(i)} \times \vec{e}_y).
\end{aligned}
\tag{2}
$$

The third term of equation (2) is the damping-like SOT with a coefficient $B_D = \frac{\mu_B \theta_{SH} J}{\gamma e M_S t_m}$ [7], where μ_B is the Bohr magneton, and θ_{SH} is an effective spin-Hall angle, and *J* is the current density, and γ is the gyromagnetic ratio, and t_m is the thickness of the AFM layer. $\vec{H}_{eff}^{(i)}$ is the effective magnetic field expressed by: $\vec{H}_{eff}^{(i)} = -\frac{1}{\mu_0 \mu} \frac{\partial H}{\partial \vec{S}^{(i)}} = \vec{H}_{ex}^{(i)} + \vec{H}_{anis}^{(i)} + \vec{H}_{DMI}^{(i)} + \vec{H}_{dipole}^{(i)}$. Here, $\vec{H}_{ex}^{(i)} = -\frac{A_{sim}}{\mu_0 \mu} (\vec{S}^{(i+1)} + \vec{S}^{(i-1)})$ is the exchange field, and $\vec{H}_{anis}^{(i)} = -\frac{2K_{sim}}{\mu_0 \mu} S_z^{(i)} \vec{e}_z$ is the anisotropy field, and $\vec{H}_{DMI}^{(i)} = -\frac{D_{sim}}{\mu_0 \mu} [(S_z^{(i+1)} - S_z^{(i-1)})\vec{e}_x + (S_x^{(i-1)} - S_x^{(i+1)})\vec{e}_z]$ is the DMI field. $\vec{H}_{dipole}^{(i)}$ is the dipole field derived as $\vec{H}_{dipole}^{(i)} = -\frac{M_S}{8\pi} \sum_j (S_y^{(j)} \vec{e}_y + S_z^{(j)} \vec{e}_z - 2S_x^{(j)} \vec{e}_x), \quad (j \neq i)$.

The Néel vector $\vec{n} = (\vec{S}^{(i)} - \vec{S}^{(i-1)})/2$ was exploited to depict AFM dynamics. The 4th Runge–Kutta method was used to solve the LLG equation with a 0.01 ps time step based on the parameters of a NiO/Pt bilayer [7]: $A_{sim} = 16$ meV, $K_{sim} = 0.04$ meV, $D_{sim} = 2$ meV, $t_m = d = 0.4$ nm, $\alpha = 0.001$, $\theta_{SH} = 0.1$, and $\mu = 3.45$ μ_B. To avoid SW reflection, an enhanced damping coefficient as a linear function of *x* is assumed at both ends of the chain [26–28]:

$$
\alpha(x)
= \begin{cases}
0.1 - \dfrac{0.099}{24} x & 0 \text{ nm} \leqslant x \leqslant 24 \text{ nm} \\
0.001 & 24 \text{ nm} < x \leqslant 1976 \text{ nm} \\
0.001 + \dfrac{0.099}{24}(x - 1976) & 1976 \text{ nm} < x \leqslant 2000 \text{ nm}
\end{cases}.
\tag{3}
$$

3. Results and discussion

We firstly investigated the inertial DW motion driven by SOT by using the collective coordinate method (CCM). The AFM staggered magnetization vector was defined as: $\vec{n} = (\vec{m}_1 - \vec{m}_2)/2M_s$, where the $\vec{m}_1$ and $\vec{m}_2$ are, respectively, the magnetizations of the two coupled sublattices with $|\vec{m}_1| = |\vec{m}_1| = M_s$ (the blue and red arrows in figure 1(a)). $\vec{n}$ was expressed in a spherical coordinate system as $\vec{n} = (\sin\theta\cos\phi, \sin\theta\sin\phi, \cos\theta)$, and a rigid-body Walker-type DW profile was introduced as $\theta(t) = 2\arctan\{\exp[(x - q(t))/\lambda]\}$, and $\phi = \phi(t)$. Here $\theta(t)$ is the polar angle for the $\vec{n}$ in the DW region, and $\phi(t)$ is the azimuthal

J. Phys. D: Appl. Phys. **55** (2022) 295302

X Ge *et al*
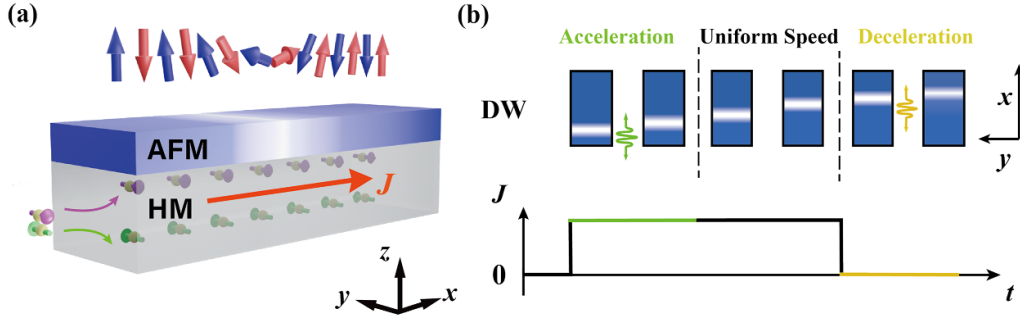
Figure 1. Bremsstrahlung-type SW excited by DW variable motion in an AFM/HM bilayer structure. (a) Schematic of an AFM/HM bilayer system and a Néel-type DW: The injected DC current *J* in the HM layer generates a transversal spin current (denoted by the purple and green arrows), which drives the AFM DW along the *x*-direction by SOT. (b) Snapshots of the DW motion. The DW accelerates (decelerates) in the rising (falling) edge of the current pulse, which is accompanied with the emission of the bremsstrahlung-type SW.

angle for the $\vec{n}$ in the DW central. $\lambda = \sqrt{\frac{A}{K}}$ is the DW width with $A = \frac{2A_{\text{sim}}}{d}$ and $K = \frac{K_{\text{sim}}}{d^3}$ the inhomogeneous exchange constant and anisotropy constant, respectively. We took into account the exchange energy, uniaxial anisotropy energy, and DMI energy, and disregarded the variation of DW width for simplicity. Using the standard σ-model procedure [29, 30], we derived the dynamics equations of q:

$$M_{\text{DW}}\ddot{q} + \frac{2S_\perp}{\gamma\lambda}G_2\dot{q} + \pi S_\perp B_{\text{D}}l\cos\phi = 0. \quad (4)$$

Here, $M_{\text{DW}} = \frac{2S_\perp}{a\gamma^2\lambda}$ is the effective mass with $S_\perp = d^2$ the cross-section area of DW and $a = \frac{5A_{\text{sim}}}{2d^3 M_s^2}$ the homogeneous exchange constants, and G_2 is the Gilbert damping parameter, and $l \approx 2M_s$ is the staggered magnetization density.

Equation (4) tells us that an AFM DW moves like a classical massive particle in the presence of frictions and external SOT force. Also, the changing of DW acceleration and velocity can trigger the variation of ϕ. However, how the DW precession is coupled to the DW acceleration is still unclear. To clarify this coupling, we further derived the dynamics equation of ϕ by considering the hard-axis anisotropy energy due to the dipole–dipole interaction and the Lorentz contraction of DW width. Under this assumption, the DW width was written as $\lambda = \sqrt{A}f^{-\frac{1}{2}}\gamma^{\frac{1}{2}}$ with $f = K - K_x\cos^2\phi$ and $\gamma = 1 - \frac{\dot{q}^2}{c^2}$. Here K_x is the hard-axis anisotropy constant, and c is the maximum group velocity. Based on the Lagrange–Rayleigh dissipation equation without the term of ϕ with an order higher than 2, the dynamics equation of ϕ can be approximately derived as:

$$\ddot{\phi} + \frac{\tilde{\alpha}_1}{2\rho}\dot{\phi} - \frac{1}{\gamma}\frac{\dot{q}\ddot{q}}{c^2}\dot{\phi} - \frac{1}{2f}\dot{\phi}^2 K_x\sin 2\phi = 0, \quad (5)$$

where $\tilde{\alpha}_1$ is the phenomenological damping factor with $\rho = \frac{A}{c^2}$.

Equation (5) indicates that the DW precession is similar to a damped pendulum. The SOT-induced DW acceleration drives the reorientation of DW magnetization (equation (4)), which offers an initial angular velocity for the DW oscillation that can be tuned by DW acceleration. This DW precession can generate a spin wave when the frequency is higher than the gap of the SW dispersion curve. On the other hand, the
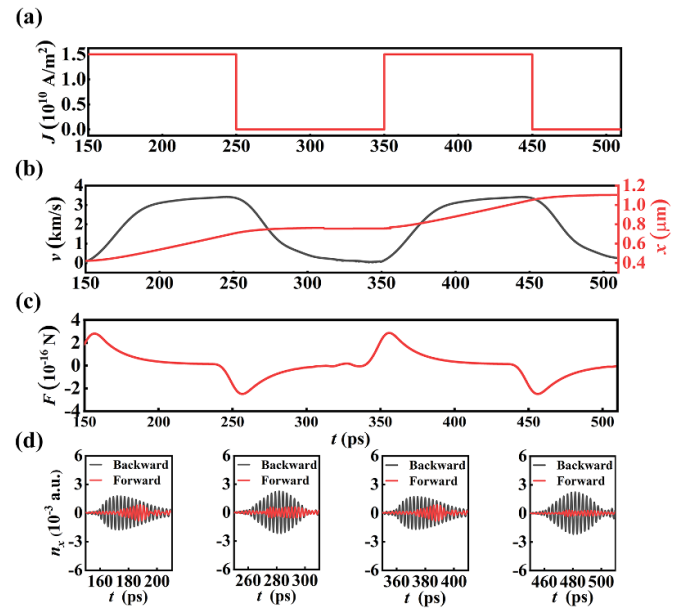

Figure 2. Typical snapshots of the DW variable motion and SW packets under the periodic pulse current. (a) Time-dependent square-wave current pulse with current density *J*. (b) DW velocity *v* and position *x*. (c) Total force on DW. (d) The *x*-component of Néel vector n_x. Here the backward and forward SWs were recorded at 128 nm to the left and 200 nm to the right of the DW center, respectively. Here $J = 1.5 \times 10^{10}$ A m^{-2}.

damping can be depressed by DW acceleration, and when the DW acceleration disappears, the DW precession will decay under damping.

Equations (4) and (5) are complicated coupled nonlinear equations, and it is highly unlikely to solve them analytically. To verify the theoretical analysis based on the CCM, we have performed the atomistic simulation. As it is shown in figure 2(a), we consider a representative SW-packet emission under a current pulse with a 0.2 ns square-wave period, a 50% duty ratio, and a 1.5×10^{10} A m^{-2} amplitude. The DW accelerates (decelerates) at the rising (falling) stage of the pulse current. This is accompanied with the SW-2 emission from both sides of DW. We recorded the n_x oscillation at 40 nm to the left and 150 nm to the right of the DW center. To precisely
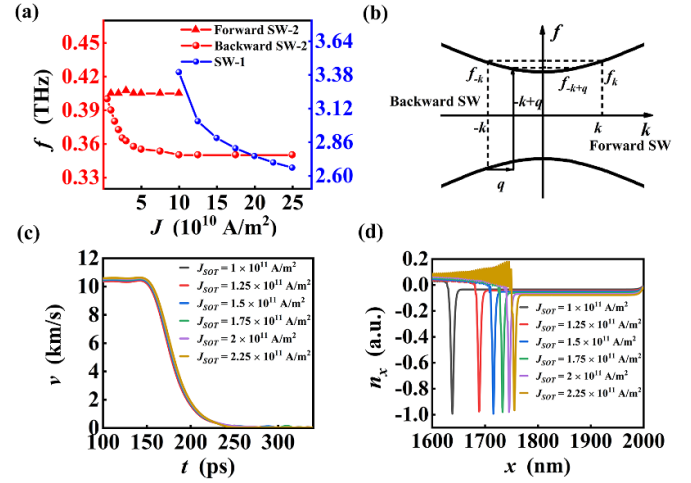
(a)

(b)
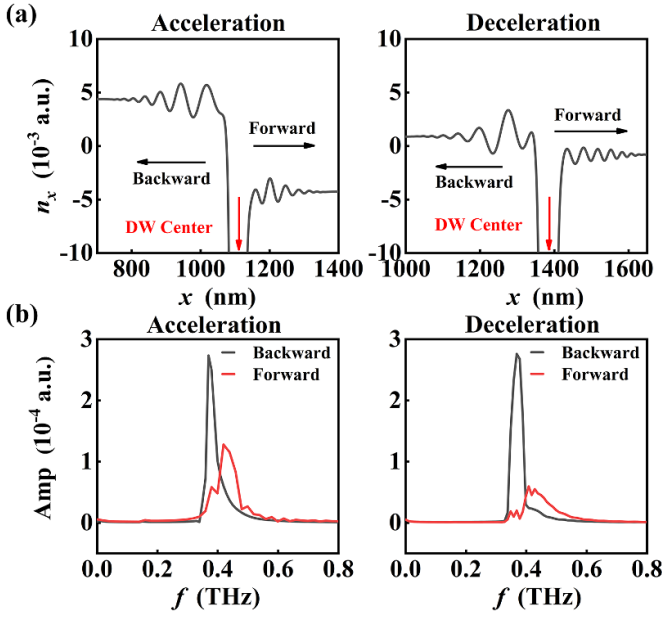
Figure 3. The bremsstrahlung-type SW emission. (a) Spatial n_x at 180 ps (DW acceleration) and 280 ps (DW deceleration). (b) Typical spectra of SWs during DW acceleration (left) and deceleration (right). Here the backward and forward SWs were recorded at 200 nm to the left and 200 nm to the right of the DW center, respectively.

(a)

(b)

(c)

(d)

Figure 4. (a) SW frequency f as a function of J. Frequency of the backward sub-THz SW-2 (the red circular-dotted line) decreases with the increase of J. When J is larger than the critical current density J_C (1×10^{11} A m^{-2}), THz SW-1 by the DW contraction is generated (blue dotted line), while the forward SW-2 diminishes. With the further increase of J, the frequency of SW-1 decreases while that of the backward SW-2 remains almost constant. (b) Dispersion curve and the schematic for the process of two-magnon emission connected by DW motion. (c) Temporal DW velocity under different J that is larger than $J_C = 1 \times 10^{11}$ A m^{-2}. (d) Spatial n_x under different J. DW profiles significantly changes with J when it is higher than 1×10^{11} A m^{-2}.

derive the n_x oscillation from a moving DW, we deleted the background fluctuation of n_x in a uniform AFM chain without any DW.

Based on equation (4) and the parameters for the simulation, the DW mass can be estimated to be approximately 2.28×10^{-30} kg. By differentiating the DW velocity with respect to t, we derived the DW acceleration, and the total force acting on DW can be determined by multiplying mass with the acceleration (figure 2(d)). One can see the total force is between 2×10^{-16} and -2×10^{-16} N. The changing of the force results from the competition between SOT and the damping effect. Furthermore, we can estimate the DW energy. Without considering the relativistic effect, the DW energy is composed of a potential energy E_p and a kinetic energy E_k. Here $E_p = 2S_\perp \sqrt{AK}$ and $E_k = \frac{1}{2}M_{DW}\dot{q}^2$. Using the simulation parameters and the stable velocity, the E_p and E_k were estimated to be $E_p = 3.6 \times 10^{-22}$ J and $E_k = 1.0 \times 10^{-23}$ J, respectively.

Figure 2(d) shows the profile of a SW-2 packet with a good repeatability under a series of current pulses. From figure 2(d), one can see that the SW-2 is emitted in the process of DW variable motion and disappears when the DW velocity becomes constant. Since the DW velocity is far below $(v_g)_{max}$, which in our case is above 10 km s^{-1}, we conclude that the mechanism of this SW-2 emission is different from that of SW-1 when the DW velocity approaches $(v_g)_{max}$ [7, 23].

Figure 3(a) exhibits the spatial n_x near the DW central. In the process of DW acceleration, the spatial symmetry of the DW profile is significantly destroyed by SOT (the left sub-figure of figure 3(a)) [7]. After the current is switched

off, however, the DW profile immediately recovers to be symmetric (the right sub-figure of figure 3(a)). The spectra of the temporal n_x for the backward and forward SW-2 in figure 2(d) were derived via fast Fourier transform (FFT), for which the sampling interval time is 0.01 ps and the sampling duration is 200 ps. Both backward and forward SW-2 exhibit a wide spectrum with a central frequency around 0.4 THz, and the frequency for the forward branch is a little higher than that of the backward one (figure 3(b)).

To further elucidate the mechanism about the bremsstrahlung-type SW-2, we deduced the SW-2 spectrum under a series of J ranging from 5×10^9 to 2.25×10^{11} A m^{-2} (figure 4(a)). We found a critical J (J_C) at 1×10^{11} A m^{-2}, below which the SW-2s are composed of the forward and backward components. The frequency for the forward branch is almost constant, while that of the backward one decreases with J for $J < J_C$ and keeps almost constant when $J > J_C$. Furthermore, we deduced the spectrum for the SW propagating along the chain (figure 4(b)). The frequency range in the dispersion curve of SW-2 is between 0.32 and 4.49 THz. Therefore, the SW-2 exhibits a frequency a little higher than the gap and a small wavenumber close to zero. This reveals that the SW-2 exhibits a typical 'magnetostatic-like' behavior.

In physics, the frequency difference between the forward and backward SW-2 can be explained based on a two-magnon emission by the interaction between an AFM DW and SW [25]. The wavenumbers of the two magnons are k and $-k + q$. Here q is the wavenumber transferred from a moving DW
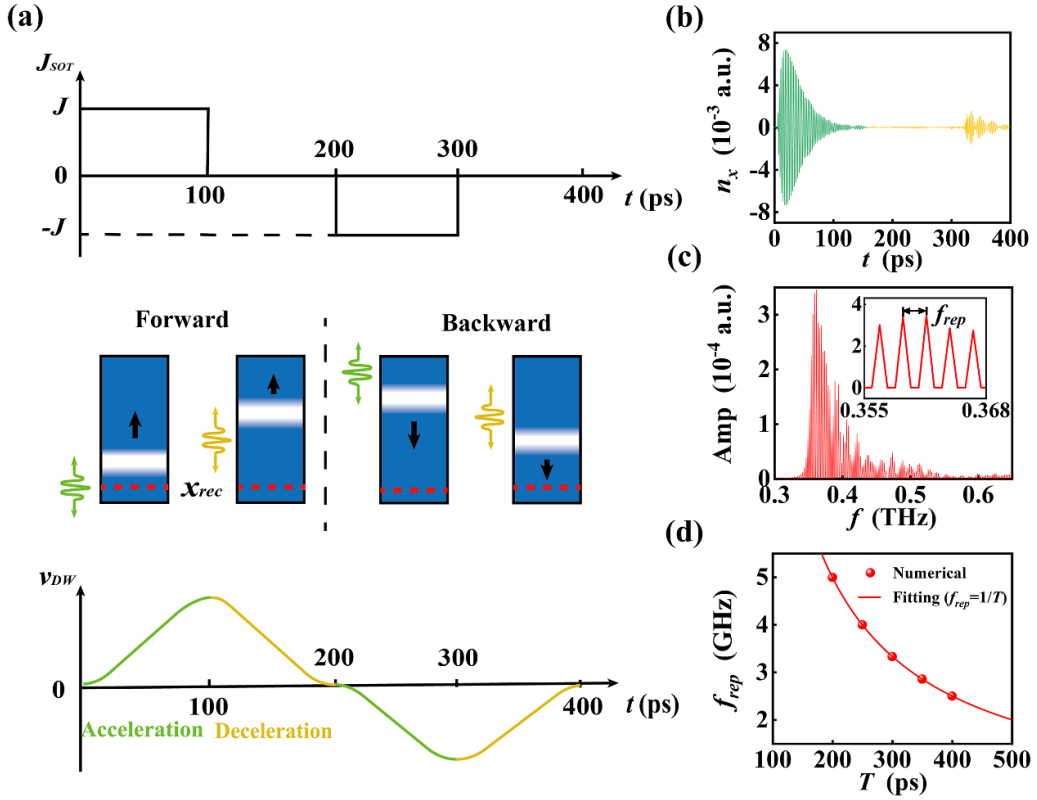
Figure 5. MFC generated by a periodic current. (a) Current density J (top), snapshots of DW motion (middle), and v_{DW} (bottom) as a function of t in a period $T = 400$ ps. The SWs in the DW acceleration and deceleration process are denoted by the green and yellow wave packets, respectively. (b) Evolution of n_x at $x = 480$ nm (the red dashed lines in figure 4(a)) in one period. (c) The spectrum of n_x in figure 4(b) under $J = 5 \times 10^{10}$ A m^{-2}. The inset is the enlarged spectrum between 0.355 and 0.368 THz with the repetition frequency $f_{rep} = 2.5$ GHz. (d) The f_{rep} of MFC at different T.

and can be estimated by $1/\lambda$, where λ is the DW width that shrinks for a moving DW due to the relativistic-like Lorentz contraction [25]. As the dispersion curve is an even function of k, the different absolute values between k and $-k + q$ leads to distinct frequencies for the two branches of SW-2. Since the wavenumber of the forward branch (k) is not influenced by q, the frequency is fixed. Nevertheless, the wavenumber of the backward SW-2 is manipulated by q. The decreasing of frequency from 0.4 to 0.35 THz corresponds to the changing of the wavenumber from -0.14 to -0.08 nm^{-1}, which is close to the variation of q (about 0.07 nm^{-1}).

When J exceeds J_C, the DW velocity approaches $(v_g)_{max}$ with a significant shrinking of DW width, which is accompanied with the disappearance of the forward SW-2 and the emission of SW-1 (the blue dotted line). The frequency of SW-1 is one magnitude higher than that of SW-2 and close to the upper limit for the frequency in the SW dispersion curve. The frequency of SW-1 decreases with the further increase of J. This SW-1 emission originates from the enhanced exchange energy by the relativistic Lorentz contraction [7, 23].

To further clarify the difference of emission mechanism for SW-1 and SW-2, we have collected the changing of DW profile and velocity when $J > J_C$ (figures 4(c) and (d)). The DW clearly shrinks with the increasing J, which is accompanied with the breaking of DW spatial symmetry and the SW-1 emission. However, the DW deceleration in the falling edge

is almost independent on J. These results illustrate that the frequency of SW-2 is mainly relevant to the variation of DW velocity. While that of SW-1 depends on the DW contraction instead of DW variable motion. This is consistent with the results in figure 2, which shows that the DW deformation does not influence the frequency of SW-2.

Finally, based on the manipulation of SW-2, we proposed the generation of a sub-THz MFC. In this work, the MFC is designed by referring the principle for an electro-optic FC [10]: we consider a continuous time-dependent signal $s(t)$, which is composed of a series of individual unit signals [$g(t)$] with a constant time-interval T with the expression given by equation (6):

$$s(t) = \sum_{n=-\infty}^{\infty} g(t - nT). \tag{6}$$

Here, n represents the serial number of the unit signal.

We introduce the Dirac comb function $\sum_{n=-\infty}^{\infty} \delta(t - nT)$ and rewrite equation (6) as:

$$s(t) = g(t) * \sum_{n=-\infty}^{\infty} \delta(t - nT). \tag{7}$$

In equation (7), the symbol * means the convolution. Using the FFT, the frequency spectrum of s is obtained as:

$$S(f) = \frac{1}{T} \sum_{n=-\infty}^{+\infty} G(f)\delta(f - \frac{n}{T}), \qquad (8)$$

where $S(f)$ and $G(f)$ is the frequency spectrum of $s(t)$ and $g(t)$, respectively. It is clear that $S(f)$ composes a series of evenly spaced frequency lines (FC) with the repetition frequency $f_{\text{rep}} = \frac{1}{T}$.

Based on this principle, we exploit a back-and-forth DW variable motion under a periodic current to generate SW packets analogous to $s(t)$ signal. The pulse protocol and snapshots of DW motion is shown in figure 5(a). In the first quarter of a period, the DW accelerates under a positive J, and the SW-2 packet is emitted towards the DW stern (the green SW packet). In the second quarter, the current is removed and the DW decelerates, exciting another SW packet towards the DW bow (the yellow SW packet). In the last two quarters, the sign of J is reversed and DW experiences a reversal acceleration and deceleration process and finally returns to its original position.

To analyze the spectrum of SW packet, we recorded the oscillation of n_x at the red dashed line in figures 5(a) and (b). This temporal n_x was converted to a MFC spectrum by FFT (figure 5(c)), for which the sampling interval is 0.01 ps, and sampling time is 1200 ps (three periods). The MFC spectrum shows that the repetition frequency f_{rep} is 2.5 GHz, and it can be manipulated between 2.5 and 5 GHz by varying T from 200 to 400 ps (figure 5(d)).

4. Conclusion

We predict the bremsstrahlung-type SW packet emitted by an AFM DW variable motion. This SW frequency is at THz and one magnitude lower than that of the SW emitted from the relativistic Lorentz contraction of the DW width when the DW velocity approaches the maximum group velocity. Based on this bremsstrahlung-type SW packet, we propose a THz MFC with a frequency interval of GHz by exploiting the back-and-forth DW variable motion driven by a pulsed current.

Data availability statement

All data that support the findings of this study are included within the article (and any supplementary files).

ORCID iDs

Shiheng Liang https://orcid.org/0000-0002-2133-2659
Yue Zhang https://orcid.org/0000-0002-1994-3071

References

[1] Chumak A V, Vasyuchka V I, Serga A A and Hillebrands B 2015 *Nat. Phys.* **11** 453461
[2] Baltz V, Manchon A, Tsoi M, Moriyama T, Ono T and Tserkovnyak Y 2018 *Rev. Mod. Phys.* **90** 015005
[3] Barman A *et al* 2021 *J. Phys.: Condens. Matter* **33** 413001
[4] Hedrich N, Wagner K, Pylypovskyi O V, Shields B J, Kosub T, Sheka D D, Makarov D and Maletinsky P 2021 *Nat. Phys.* **17** 574–7
[5] Kim S K, Tserkovnyak Y and Tchernyshyov O 2014 *Phys. Rev.* B **90** 104406
[6] Tveten E G, Qaiumzadeh A and Brataas A 2014 *Phys. Rev. Lett.* **112** 147204
[7] Shiino T, Oh S H, Haney P M, Lee S W, Go G, Park B G and Lee K J 2016 *Phys. Rev. Lett.* **117** 087203
[8] Picqué N and Hänsch T W 2019 *Nat. Photon.* **13** 146–57
[9] Wu M, Kalinikos B A, Carr L D and Patton C E 2006 *Phys. Rev. Lett.* **96** 187202
[10] Rueda A, Sedlmeir F, Kumari M, Leuchs G and Schwefel H G L 2019 *Nature* **568** 378–81
[11] Richardson D, Kalinikos B A, Carr L D and Wu M 2018 *Phys. Rev. Lett.* **121** 107204
[12] Burghoff D, Kao T, Han N, Chan C W I, Cai X, Yang Y, Hayton D J, Gao J R, Reno J L and Hu Q 2014 *Nat. Photon.* **8** 462–7
[13] Zhou Z, Wang X, Nie Y, Xia Q and Guo G 2021 *J. Magn. Magn. Mater.* **534** 168046
[14] Wang Z, Yuan H Y, Cao Y, Li Z-X, Duine R A and Yan P 2021 *Phys. Rev. Lett.* **127** 037202
[15] Qiu X, Legrand W, He P, Wu Y, Yu J, Ramaswamy R, Manchon A and Yang H 2016 *Phys. Rev. Lett.* **117** 217206
[16] Yang H, Yuan H Y, Yan M, Zhang H W and Yan P 2019 *Phys. Rev.* B **100** 024407
[17] Chen F, Zhang Z D, Luo W, Yang X F, You L and Zhang Y 2020 *J. Magn. Magn. Mater.* **511** 166995
[18] Selzer S, Atxitia U, Ritzmann U, Hinzke D and Nowak U 2016 *Phys. Rev. Lett.* **117** 107201
[19] Yanes R, Rosa M R and Lopez-Diaz L 2020 *Phys. Rev.* B **102** 134424
[20] Schlickeiser F, Ritzmann U, Hinzke D and Nowak U 2014 *Phys. Rev. Lett.* **113** 097201
[21] Shen P, Tserkovnyak Y and Kim S K 2020 *J. Appl. Phys.* **127** 223905
[22] Caretta L, Oh S H, Lee D K, Lee B H, Kim S K, Ross C A, Lee K J and Beach G S D 2020 *Science* **370** 1438–42
[23] Oh S H, Kim S K, Lee D K, Go G, Kim K J, Ono T, Tserkovnyak Y and Lee K J 2018 *Phys. Rev.* B **97** 139901
[24] Chen F, Ge X, Luo W, Xing R H, Liang S H, Yang X F, You L, Xiong R, Otani Y and Zhang Y 2021 *Phys. Rev. Appl.* **15** 014030
[25] Tatara G, Akosa C A and de Zuazola R M O 2020 *Phys. Rev. Res.* **2** 043226
[26] Consolo G, Lopez-Diaz L, Torres L and Azzerboni B 2007 *Phys. Rev.* B **75** 214428
[27] Yang J, Yoo M-W and Kim S-K 2015 *J. Appl. Phys.* **118** 163902
[28] Zhang B, Wang Z, Cao Y, Yan P and Wang X R 2018 *Phys. Rev.* B **97** 094421
[29] Tveten E G, Qaiumzadeh A, Tretiakov O A and Brataas A 2013 *Phys. Rev. Lett.* **110** 127208
[30] Tveten E G, Müller T, Linder J and Brataas A 2016 Intrinsic magnetization of antiferromagnetic textures *Phys. Rev.* B **93** 104408